



Highly sensitive gas refractive index sensor based on hollow-core photonic bandgap fiber

ZHE ZHANG,^{1,2} JUN HE,^{1,2,*}  BIN DU,^{1,2} KUIKUI GUO,^{1,2} AND YIPING WANG^{1,2}

¹Guangdong and Hong Kong Joint Research Centre for Optical Fiber Sensors, College of Physics and Optoelectronic Engineering, Shenzhen University, Shenzhen 518060, China

²Key Laboratory of Optoelectronic Devices and Systems of Ministry of Education and Guangdong Province, Shenzhen University, Shenzhen 518060, China

*hejun07@szu.edu.cn

Abstract: A highly sensitive gas refractive index (RI) sensor based on hollow-core photonic bandgap fiber (HC-PBF) and Fourier transform white-light interferometry was experimentally demonstrated. HC-PBFs with lower loss than hollow silica tubes render a longer air cavity for the Fabry-Perot interferometers (FPIs) without a great deal of compromise to the fringe visibility of interference. Fourier transform phase demodulation method was employed in the experiment and a directly proportional relationship between the phase sensitivity and cavity length was demonstrated. For a cavity length of ~ 24.9 mm, the sensor's gas RI sensitivity reaches up to $50775.54 \mu\text{m}/\text{RIU}$ in an air RI range from 1.000 to 1.030. Considering the cavity length demodulation resolution of $0.06 \mu\text{m}$ achieved by this method, the sensor can detect gas RI change with a resolution of 10^{-6} RIU, which can meet the sensing demand for almost all the gases. Moreover, the gas RI sensitivity and measurement range can be improved further by lengthening the HC-PBF. The high sensitivity, large dynamic range and good linearity of the proposed sensor make it a good candidate for biosensing, monitoring of modern chemical industry or gas laser systems.

© 2019 Optical Society of America under the terms of the [OSA Open Access Publishing Agreement](#)

1. Introduction

Precise determination of refractive index (RI) is of great significance in many fields such as label-free chemical and biomedical sensing [1,2]. Owing to their compact size, optical fiber RI sensors have been widely studied and reported, such as fiber surface Bragg gratings [3], microfiber Bragg gratings [4], long-period fiber gratings [5,6], fiber Mach-Zehnder interferometers [7,8], fiber Fabry-Perot interferometers (FPIs) [9], fiber Michelson interferometers [10], fiber surface plasmon resonance sensors [11,12] and liquid-modified photonic crystal fiber directional couplers [13]. However, developed for chemical and biological applications, the most reported optical fiber RI sensors are designed for aquatic environment, namely the RI measurement range are around 1.33 [14], which suffers an extremely low sensitivity for gas RI measurements. The measurement of gas RI, which is around 1.0, is of great significant in many fields such as chemical industries (i.e. the detection of flammable, explosion, and toxic gases [15,16]), modern optical instruments and gas lasing systems [17,18,19], where high-power laser beams propagate in and interact with gaseous media. Recently, several optical fiber gas RI measurement schemes have been reported, the most typical case is open-cavity FPIs [20], the RI sensitivities of which are around $1053.44 \text{ nm}/\text{RIU}$. By employing Vernier effect in the open-cavity FPIs, the RI sensitivities can be enhanced up to $30899 \text{ nm}/\text{RIU}$ [21]. However, the sensitivity of an FPI can hardly be enhanced further, using the traditional wavelength demodulation method. Moreover, the wavelength demodulation method, characterized by tracking a peak or dip wavelength, is not an absolute but a relative measurement of RI, which needs to be calibrated to the standard RI.

Fourier transform white-light interferometry has been widely used to interrogate the absolute optical path or phase difference, which can be employed to determine the absolute RI of gas diffused into the interferometer. Phase detection is an ultrasensitive detection method that has been widely employed for probing extremely weak signals [22]. For FPI sensors, the phase sensitivity is in direct proportion to the cavity length due to the phase accumulating effects. However, all the aforementioned open-cavity FPI gas RI sensors suffer a limited cavity length due to the poor optical transmission properties of the FPI cavity. Thus, a low-loss hollow core fiber will be advantageous to a long cavity FPI. Hollow-core photonic bandgap fibers (HC-PBFs) can simultaneously confine the propagating lights and gas into the hollow core and the transmission loss is typically ~ 1.2 dB/km [23], which enables long-distance interaction of light and gas [24], offering an excellent low-loss cavity for gas RI measurements. A minor change of gas RI will result in a relatively large optical phase change, which is proportional to the HC-PBF length.

Herein, we reported on the highly sensitive absolute measurement of gas RI based on HC-PBF open-cavity FPI. Fourier transform white-light interferometry was used in the experiments and the gas RI sensitivities can reach up to $50775.54 \mu\text{m}/\text{RIU}$ with a 24.9 mm-long HC-PBF cavity. Considering the OPD demodulation resolution of $0.06 \mu\text{m}$ by this algorithm [25], the sensor can detect gas RI change with a resolution of 10^{-6} RIU. A directly proportional relationship between the gas RI sensitivity and the cavity length of HC-PBF was demonstrated both theoretically and experimentally, namely the gas RI sensitivity can be improved further by employing a longer HC-PBF cavity. The proposed sensor is compact in size and free of electromagnetic interference, and hence may find vital applications in biosensing, chemical industry or modern gas laser systems monitoring as well as dynamic acoustic pressure detection.

2. Sensor fabrication and working principles

The illustrative configuration of the proposed sensor is shown in Fig. 1(a). At first, a section of HC-PBF (NKT, HC-1550-02) was spliced with a lead-in single-mode fiber (SMF, Corning, SMF-28) with a commercial arc fusion splicer (Fujikura, FSM-60S) and optimized discharge parameters to avoid the collapse of hollow cores. The air core diameter of the employed HC-PBF is $\sim 10.9 \mu\text{m}$ and the insertion loss of a fusion joint is ~ 2.6 dB. Then, the HC-PBF was cut off with a homemade microscope-assisted fiber cutter [26,27] to accurately control the length of reserved HC-PBF. A section of silica hollow core fibers (HCFs) was fusion spliced with the HC-PBF, and the other end of the HCF was sliced with a tilt angle to eliminate the parasitic interference generated from the end facet reflection. The inner diameter and outer diameter of the employed HCF are $\sim 2 \mu\text{m}$ and $\sim 125 \mu\text{m}$, respectively. The cross-sectional SEM images of the employed HC-PBF and the HCF are shown in Fig. 2, respectively. The difference in the core diameters of HC-PBF and HCF enables a reflector and a microfluidic channel for gas into the HC-PBF cavity simultaneously. Thus, an open-cavity FPI was formed. It is worth noting that, HCFs with larger inner diameter can render a faster gas RI response while reducing the reflective intensity of the second reflector and thus the fringe contrast. Alternatively, the response time of the sensor can be improved by shortening the length of HCF. So HCFs with an inner diameter of $\sim 2 \mu\text{m}$ was employed in our experiments.

The low transmission loss of HC-PBFs enables an open long air cavity without a vast sacrificing of the visibility of fringe pattern. Four HC-PBF FPI sensors (S_1 , S_2 , S_3 , and S_4) with different HC-PBF length, i.e. $107 \mu\text{m}$, 1.1 mm, 2.1 mm and 12.3 mm, were fabricated, respectively. The reflection spectra of these sensors were measured with a broadband light source (BBS), a 3 dB fiber coupler and an optical spectrum analyzer (OSA) (Yokogawa, AQ6370C) with a resolution of 0.02 nm. As shown in Fig. 3, the free spectrum range (FSR) of the reflection spectra is narrowing with the increasing of HC-PBF length, which agree well with the relationship

$$FSR = \frac{\lambda_1 \lambda_2}{2nL}, \quad (1)$$

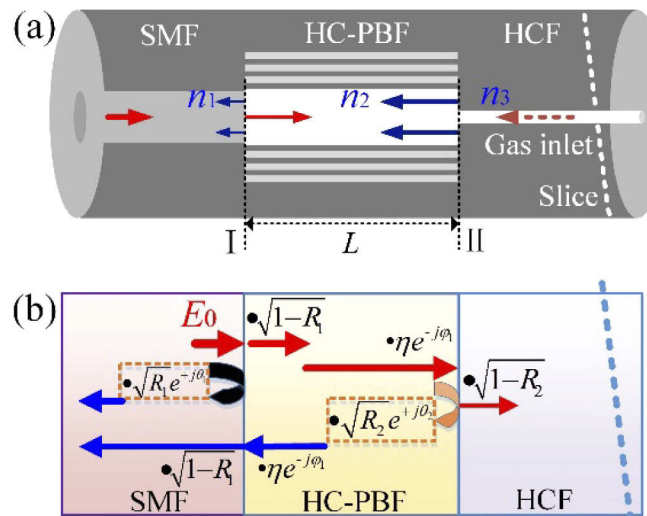


Fig. 1. Schematic diagram of the proposed sensor with (a) structure and (b) working principle.

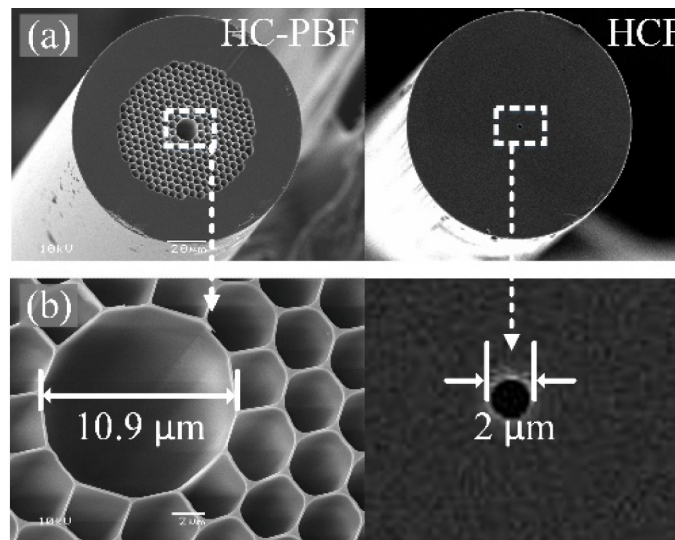


Fig. 2. (a) Cross-sectional SEM images of the employed HC-PBF and HCF and (b) locally enlarged view of the air holes in the centers of HC-PBF and HCF.

where λ_1 , λ_2 are the adjacent dip wavelength, n and L are the RI of air, the HC-PBF length, respectively. The decrease in fringe contrast with the cavity lengthening can be attributed to the transformation of light-guiding mechanism in the HC-PBF cavity. To be specific, when the HC-PBF is short enough, the photonic bandgap (PBG) guiding mechanism of the HC-PBF doesn't work and the light transmits in the air cavity and is spatially coupled back to the lead-in SMF. Thus, the mode-mismatch-induced insertion loss of the splicing joint has little effect on the reflected light intensity of the second mirror. With the lengthening of HC-PBF, the PBG effect become dominant and the light suffers a mode-mismatch-induced splicing loss of ~ 2.6 dB, resulting in a decreased fringe contrast compared with a shorter HC-PBF. When the HC-PBF

is longer enough, the fringe contrast will not decrease significantly. As shown in Fig. 1(a), the proposed open-cavity FPI has two main reflection surfaces (I and II). The reflectivity of the two surfaces R_1 and R_2 can be calculated by

$$R_1 = \frac{(n_1 - n_2)^2}{(n_1 + n_2)^2}, R_2 = \frac{(n_2 - n_3)^2}{(n_2 + n_3)^2}, \quad (2)$$

where n_1 , n_2 and n_3 are about 1.46, 1.00 and 1.45, respectively. The reflectivity of the two

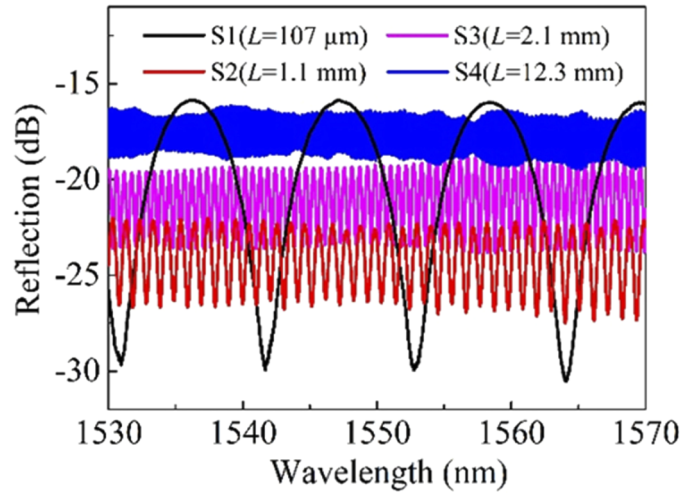


Fig. 3. Reflection spectra of four fabricated sensors (S_1 , S_2 , S_3 , and S_4) with different HC-PBF length, i.e. 107 μm , 1.1 mm, 2.1 mm and 12.3 mm, respectively.

surfaces R_1 and R_2 can be calculated to be ~ 0.035 and 0.034 , respectively. Since the reflectivity is low ($R \ll 1$), the proposed sensor consists of a low-finesse Fabry-Perot cavity. High-order reflections in the cavity are negligible and the interference spectrum of the FPI can then be simply described by the two-wave interference approximation [28]. The reflection in the FPI cavity is schematically illustrated in Fig. 1(b), where E_0 is the field intensity of incident light, η is the transmission coefficient of the FPI cavity, φ_1 is the phase change after transmitting through the cavity and θ_1 , θ_2 are the phase change of the incident light after transmitting through the interfaces of air/silica and silica/air, respectively. The total intensity of reflection light can be expressed as

$$I(\lambda) = I_0 [R_1 + R_2 \eta - 2\sqrt{R_1 R_2 \eta} \cos(\frac{2\pi}{\lambda} nL + \varphi_0)], \quad (3)$$

where I_0 , n , L and φ_0 denote the light intensity launched into the Fabry-Perot cavity, the RI of air, the cavity length and the initial phase difference of the two beams, respectively. For HC-PBFs, the transmission loss is small and $\eta \approx 1$. From Eq. (3), we can see that the FPI exhibits a reflection spectrum approximating a sinusoidal curve. The phase difference of the two beams can be expressed in the optical path difference (OPD) of the two beams. The OPD can be expressed as

$$OPD = 2n(P, T)L, \quad (4)$$

where L is the cavity length and $n(P, T)$ is the RI of gas. For the standard air, the RI can be expressed as a function of the pressure P (Pa), the temperature T ($^{\circ}\text{C}$) according to [29]

$$n = 1 + \frac{2.8793 \times 10^{-9}}{1 + 0.00367 \times T} P. \quad (5)$$

When the RI of gas varies, the OPD changes accordingly. Namely if we extract the information of

OPD from the spectra, the RI of gas can be determined. The RI sensitivity S can be expressed as

$$S = \frac{\delta(OPD)}{\delta(n)} = 2L, \quad (6)$$

which is in direct proportion to the cavity length L . This is the fundamental working principle of the proposed gas RI sensor. Figure 4 exhibits the calculated gas RI sensitivity of the proposed sensors with different cavity length L using Eqs. (4) and (6). It is obvious that the OPD increases

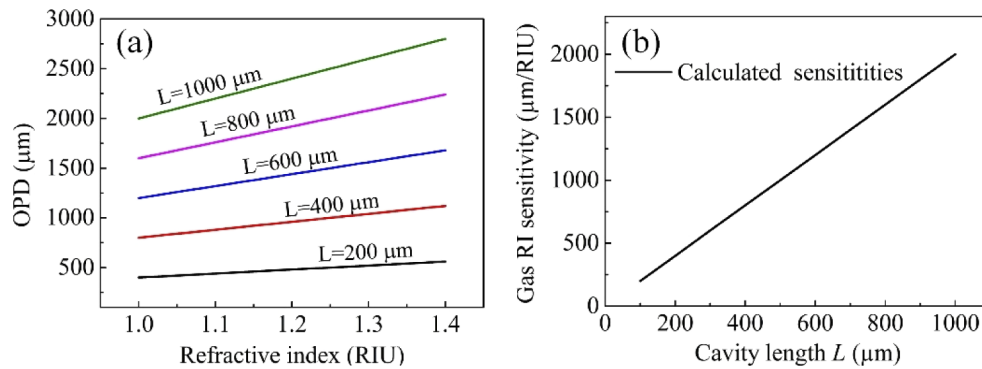


Fig. 4. (a) Calculated OPDs of FPIs with different cavity length L as functions of the gas RI; (b) Calculated gas RI sensitivities as a function of FPI cavity length L .

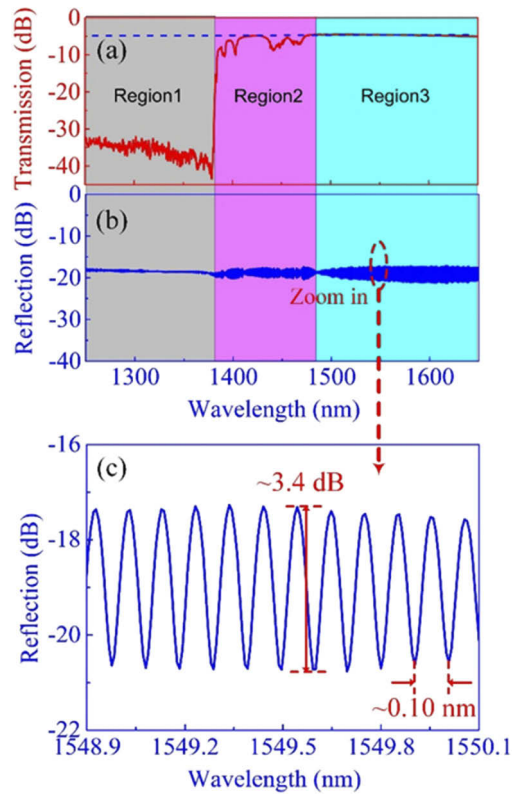


Fig. 5. (a) Measured transmission spectrum and (b) reflection spectra of the FPI with a 12.3 mm length HC-PBF; (c) Enlarged view of the FPI reflection spectrum at ~1550 nm.

with an increasing RI, and the RI sensitivity of the *OPD* increases linearly with an increasing cavity length L .

Figure 5(a) shows the measured transmission spectrum of the employed HC-PBF with a length of ~ 12.3 mm, where three typical regions in the wavelength range of 1250-1650 nm, named Region 1, 2 and 3, are clearly presented. In Region 1, which is beyond the photonic bandgap of HC-PBF, almost all of the optical energy is leaking out. By contrast, within the photonic bandgap of HC-PBF, i.e. Region 2 and 3, light propagates through HC-PBFs with low loss. Figure 5(b) shows the reflection spectrum of a fabricated HC-PBF FPI sensor (sample S_4) with a cavity length of ~ 12.3 mm and Fig. 5(c) exhibits an enlarged view of Fig. 5(b) at ~ 1550 nm. It can be clearly seen that, within the photonic bandgap range (Region 2 and 3), the fringe visibility was ~ 3.4 dB, whereas it decreased to less than 0.5 dB beyond the photonic bandgap of HC-PBF (Region 1). This is the reason why we choose HC-PBF to construct the open cavity of the FPI.

3. Air RI sensing response of the proposed HC-PBF FPI sensors

The air RI test setup and optical spectra acquisition device are schematically shown in Fig. 6(b). Four fabricated sensor samples S_1 - S_4 , which have a cavity length L of 107 μm , 1.1 mm, 2.1 mm and 12.3 mm, respectively, were placed into an air chamber. A commercial air pressure

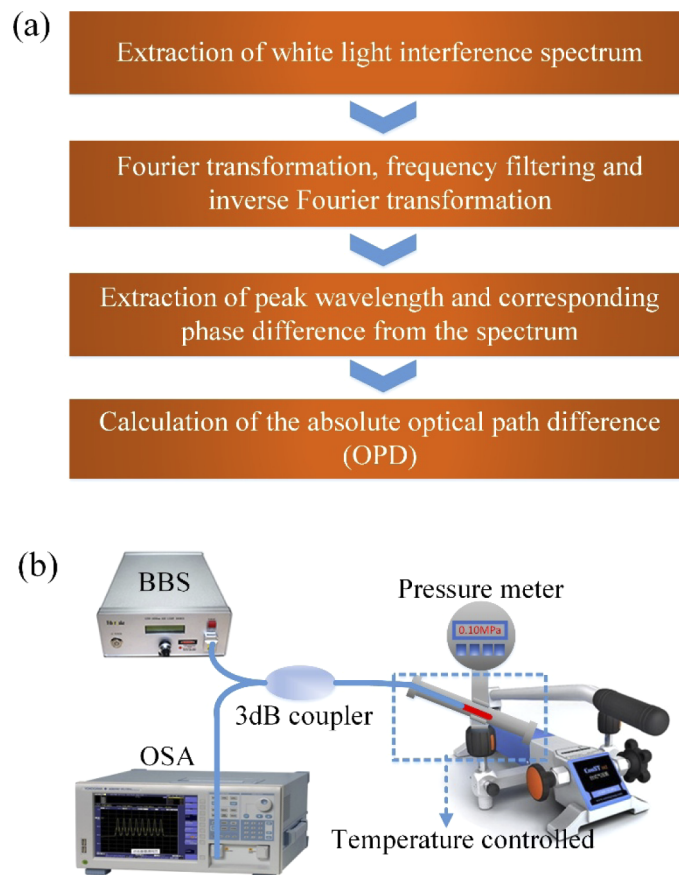


Fig. 6. (a) Flow chart of the employed Fourier phase demodulation method. (b) Air RI test setup and optical spectra acquisition device (BBS: broadband light source, OSA: optical spectrum analyzer).

generator with a stability of ± 0.2 KPa was employed with a high-precision digital pressure meter (ConST-811). The chamber was kept at a constant temperature of 25 °C and was fitted with a feed-through and sealed by strong glue to extend the fiber pigtail outside the chamber for real-time measurements. The resolution of OSA was set to 0.02 nm. The air RI was increased from 1.00026 to 1.01056 in a step of 0.00132, corresponding to air pressure in the chamber elevated from atmosphere pressure (0.1 MPa) to 4.0 MPa in a step of 0.5 MPa according to Eq. (5) at 25 °C. At each measured point, the pressure was kept for 1 min and the temperature was controlled at 25 °C during the whole measurement process. After holding the air pressure for 1 min, the reflection spectra of the samples were recorded by the OSA. Each recorded reflection spectra was demodulated by the Fourier phase method as reported in Ref. [25] and [30]. Figure 6(a) presents a flow chart of the employed Fourier phase demodulation method. The *OPD* change of the HC-PBF FPI sensor samples S_1 , S_2 , S_3 , and S_4 with respect to the air RI were illustrated in Figs. 7(a), 7(b), 7(c), and 7(d), respectively. The air RI sensitivities (measured from the linear fits of the *OPDs* as functions of air RIs, as shown in Fig. 7) of the four samples S_1 , S_2 , S_3 , and S_4 were 208.245, 2276.091, 3839.792, 23364.642 $\mu\text{m}/\text{RIU}$, respectively. Note that the air RI sensitivity of the proposed sensors exhibits a positive correlation with the cavity length L .

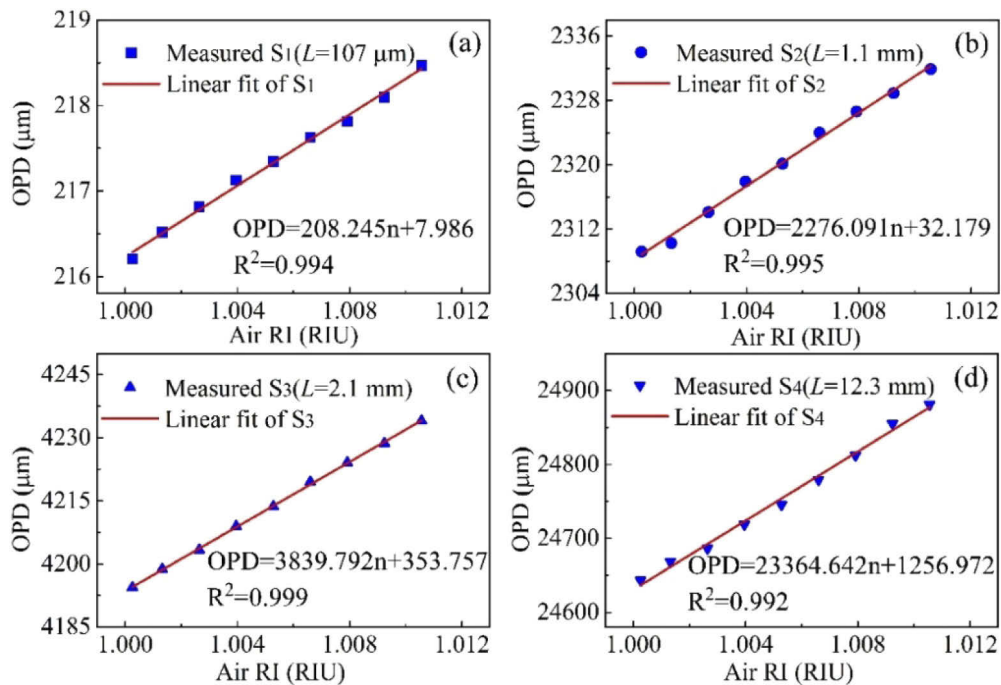


Fig. 7. Demodulated *OPDs* of four HC-PBF FPI sensor samples S_1 , S_2 , S_3 , and S_4 as functions of the air RI in a range of 1.00026 to 1.01056. (a) S_1 ($L = 107 \mu\text{m}$), (b) S_2 ($L = 1.1 \text{ mm}$), (c) S_3 ($L = 2.1 \text{ mm}$), and (d) S_4 ($L = 12.3 \text{ mm}$).

Furthermore, we investigated the air RI response of the proposed HC-PBF FPI sensor in a larger air pressure range from 0.1 to 10 MPa, corresponding to air RI from 1.00026 to 1.02640. Another four HC-PBF FPI sensor samples (S_5 , S_6 , S_7 , and S_8) with cavity length L of 2.7, 6.7, 12.4 and 24.9 mm, respectively, were fabricated and tested by employing the same equipment and method as described above. The *OPD* demodulation results of S_5 , S_6 , S_7 , and S_8 obtained by Fourier phase method were shown in Figs. 8(a), 8(b), 8(c), and 8(d), respectively, where linear fits were employed with high linearity of 0.999, 0.998, 0.999 and 0.999. It is obvious that the RI sensitivities of the samples S_5 - S_8 are also of positive relevance with its cavity length L ,

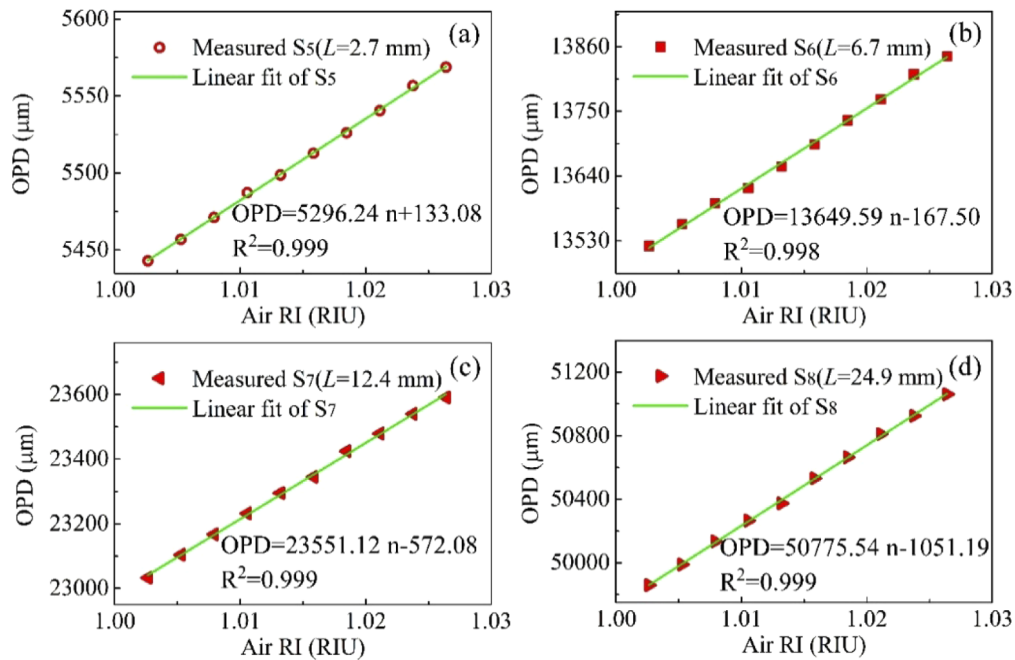


Fig. 8. Demodulated OPDs of four HC-PBF FPI sensor samples S_5 , S_6 , S_7 , and S_8 as functions of the air RI in a range of 1.00026 to 1.02640. (a) S_5 ($L = 2.7$ mm), (b) S_6 ($L = 6.7$ mm), (c) S_7 ($L = 12.4$ mm), and (d) S_8 ($L = 24.9$ mm).

which agrees well with the theoretical predictions shown in Fig. 3(a). It should be noted that, the maximum cavity length is limited by the wavelength resolution of the employed OSA. To be specific, the FSR of the sensor should be larger than the wavelength resolution of the OSA (~ 0.02 nm). Therefore, the maximum cavity length in our case is calculated to be 60 mm. Figure 9 exhibits the measured air RI sensitivities of the eight HC-PBF FPI sensor samples (i.e. S_1 - S_8) fabricated in this work as a function of their cavity lengths L . Theoretical calculations using Eq. (6) were also demonstrated in Fig. 9. It is clear that the experimental results agree well with

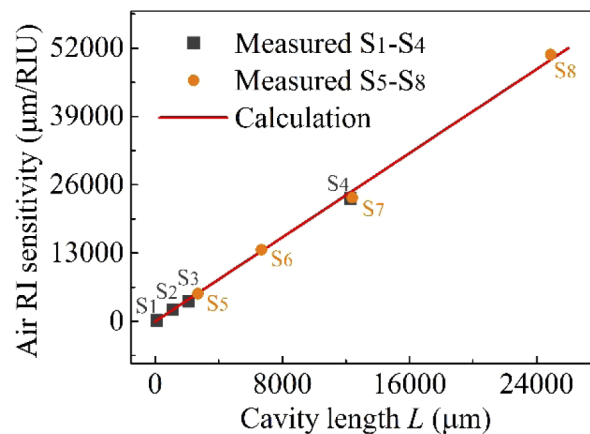


Fig. 9. The air RI sensitivity of eight HC-PBF FPI sensors (S_1 - S_8) as a function of the cavity length L .

the theoretical calculations. The small deviation may result from the measurement error in the cavity length L . Moreover, it is worth noting that, the proposed sensor can render a wider air RI measurement range, which was not explored in the experiments due to the limitation of our test equipment. Anyway, we believe that the proposed HC-PBF FPI air RI sensor could find vital applications in modern biochemical sensing, lasing industry and dynamic acoustic detection.

4. Conclusion

We experimentally demonstrated a highly sensitive gas RI sensor based on a long air-cavity HC-PBF FPI and optical phase demodulation method. A high gas RI sensitivity of 50775.54 $\mu\text{m}/\text{RIU}$ in a RI range from 1.000 to 1.030 was achieved for the sensor with cavity length L of ~ 24.9 mm. A positive proportionality between the gas RI sensitivity and cavity length L was proved both theoretically and experimentally. The proposed long air-cavity HC-PBF FPI gas RI sensor exhibits ultrahigh sensitivity, large dynamic range, excellent linearity and repeatability. Therefore, this novel type of gas RI sensor may find vital applications in the biochemical industry for noxious gas detect, pressure control and modern gas laser systems for gas nonlinearity research. Moreover, dynamic acoustic detection with the proposed gas RI sensor is also a promising research focus and will be studied in the future.

Funding

National Natural Science Foundation of China (61875128, 91860138, 61635007); Shenzhen Science and Technology Innovation Commission (JCYJ20180507182058432, JCYJ20160427104925452); Development and Reform Commission of Shenzhen Municipality.

Disclosures

The authors declare no conflicts of interest.

References

1. A. Leung, P. Mohana Shankar, and R. Mutharasan, "A review of fiber-optic biosensors," *Sens. Actuators, B* **125**(2), 688–703 (2007).
2. X. Fan, I. White, S. Shopova, H. Zhu, J. Suter, and Y. Sun, "Sensitive optical biosensors for unlabeled targets: A review," *Anal. Chim. Acta* **620**(1-2), 8–26 (2008).
3. C. Lin, C. Liao, J. Wang, J. He, Y. Wang, Z. Li, T. Yang, F. Zhu, K. Yang, Z. Zhang, and Y. Wang, "Fiber surface Bragg grating waveguide for refractive index measurements," *Opt. Lett.* **42**(9), 1684–1687 (2017).
4. X. Fang, C. Liao, and D. Wang, "Femtosecond laser fabricated fiber Bragg grating in microfiber for refractive index sensing," *Opt. Lett.* **35**(7), 1007–1009 (2010).
5. J. Tang, S. Cheng, W. Hsu, T. Chiang, and L. Chau, "Fiber-optic biochemical sensing with a colloidal gold-modified long period fiber grating," *Sens. Actuators, B* **119**(1), 105–109 (2006).
6. L. Qi, C. Zhao, J. Yuan, M. Ye, J. Wang, Z. Zhang, and S. Jin, "Highly reflective long period fiber grating sensor and its application in refractive index sensing," *Sens. Actuators, B* **193**, 185–189 (2014).
7. Z. Li, C. Liao, Y. Wang, X. Dong, S. Liu, K. Yang, and J. Zhou, "Ultrasensitive refractive index sensor based on a Mach-Zehnder interferometer created in twin-core fiber," *Opt. Lett.* **39**(17), 4982–4985 (2014).
8. S. Zhang, W. Zhang, P. Geng, and S. Gao, "Fiber Mach-Zehnder interferometer based on concatenated down-and up-tapers for refractive index sensing applications," *Opt. Commun.* **288**, 47–51 (2013).
9. R. Gao, Y. Jiang, W. Ding, Z. Wang, and D. Liu, "Filmed extrinsic Fabry-Perot interferometric sensors for the measurement of arbitrary refractive index of liquid," *Sens. Actuators, B* **177**, 924–928 (2013).
10. H. Meng, W. Shen, G. Zhang, X. Wu, W. Wang, C. Tan, and X. Huang, "Michelson interferometer-based fiber-optic sensing of liquid refractive index," *Sens. Actuators, B* **160**(1), 720–723 (2011).
11. J. Zhao, S. Cao, C. Liao, Y. Wang, G. Wang, X. Xu, C. Fu, G. Xu, J. Lian, and Y. Wang, "Surface plasmon resonance refractive sensor based on silver-coated side-polished fiber," *Sens. Actuators, B* **230**, 206–211 (2016).
12. S. Cao, Y. Shao, Y. Wang, T. Wu, L. Zhang, Y. Huang, F. Zhang, C. Liao, J. He, and Y. Wang, "Highly sensitive surface plasmon resonance biosensor based on a low-index polymer optical fiber," *Opt. Express* **26**(4), 3988–3994 (2018).
13. C. Lin, C. Liao, Y. Zhang, L. Xu, Y. Wang, C. Fu, K. Yang, J. Wang, J. He, and Y. Wang, "Optofluidic gutter oil discrimination based on a hybrid-waveguide coupler in fiber," *Lab Chip* **18**(4), 595–600 (2018).

14. X. Wang and O. Wolfbeis, "Fiber-optic chemical sensors and biosensors (2013–2015)," *Anal. Chem.* **88**(1), 203–227 (2016).
15. N. Liu, M. Tang, M. Hentschel, H. Giessen, and A. Alivisatos, "Nanoantenna-enhanced gas sensing in a single tailored nanofocus," *Nat. Mater.* **10**(8), 631–636 (2011).
16. A. Andringa, C. Piliago, I. Katsouras, P. Blom, and D. Leeuw, "NO₂ detection and real-time sensing with field-effect transistors," *Chem. Mater.* **26**(1), 773–785 (2014).
17. P. Corkum, C. Rolland, and T. Rao, "Supercontinuum generation in gases," *Phys. Rev. Lett.* **57**(18), 2268–2271 (1986).
18. A. Couairon, M. Franco, A. Mysyrowicz, J. Biegert, and U. Keller, "Pulse self-compression to the single-cycle limit by filamentation in a gas with a pressure gradient," *Opt. Lett.* **30**(19), 2657–2659 (2005).
19. T. Pitts, T. Luk, J. Gruetzner, T. Nelson, A. McPherson, S. Cameron, and A. Bernstein, "Propagation of self-focusing laser pulses in atmosphere: experiment versus numerical simulation," *J. Opt. Soc. Am. B* **21**(11), 2008–2016 (2004).
20. M. Ferreira, L. Coelho, K. Schuster, J. Kobelke, J. Santos, and O. Frazão, "Fabry–Perot cavity based on a diaphragm-free hollow-core silica tube," *Opt. Lett.* **36**(20), 4029–4031 (2011).
21. M. Quan, J. Tian, and Y. Yao, "Ultra-high sensitivity Fabry–Perot interferometer gas refractive index fiber sensor based on photonic crystal fiber and Vernier effect," *Opt. Lett.* **40**(21), 4891–4894 (2015).
22. G. Gagliardi, M. Salza, S. Avino, P. Ferraro, and P. Natale, "Probing the ultimate limit of fiber-optic strain sensing," *Science* **330**(6007), 1081–1084 (2010).
23. P. Roberts, F. Couny, H. Sabert, B. Mangan, D. Williams, L. Farr, M. Mason, A. Tomlinson, T. Birks, J. Knight, and P. Russell, "Ultimate low loss of hollow-core photonic crystal fibers," *Opt. Express* **13**(1), 236–244 (2005).
24. W. Jin, H. Xuan, and H. Ho, "Sensing with hollow-core photonic bandgap fibers," *Meas. Sci. Technol.* **21**(9), 094014 (2010).
25. Y. Jiang, "Fourier transform white-light interferometry for the measurement of fiber-optic extrinsic Fabry–Perot interferometric sensors," *IEEE Photonics Technol. Lett.* **20**(2), 75–77 (2008).
26. Z. Zhang, C. Liao, J. Tang, Y. Wang, Z. Bai, Z. Li, K. Guo, M. Deng, S. Cao, and Y. Wang, "Hollow-core-fiber-based interferometer for high-temperature measurements," *IEEE Photonics J.* **9**(2), 1–9 (2017).
27. Z. Zhang, J. He, Q. Dong, Z. Bai, C. Liao, Y. Wang, S. Liu, K. Guo, and Y. Wang, "Diaphragm-free gas-pressure sensor probe based on hollow-core photonic bandgap fiber," *Opt. Lett.* **43**(13), 3017–3020 (2018).
28. J. Ma, "Miniature fiber-tip Fabry-Perot interferometric sensors for pressure and acoustic detection [D]," The Hong Kong Polytechnic University, (2014).
29. M. Deng, C. Tang, T. Zhu, Y. Rao, L. Xu, and M. Han, "Refractive index measurement using photonic crystal fiber-based Fabry-Perot interferometer," *Appl. Opt.* **49**(9), 1593–1598 (2010).
30. Z. Zhang, J. He, B. Du, F. Zhang, K. Guo, and Y. Wang, "Measurement of high pressure and high temperature using a dual-cavity Fabry–Perot interferometer created in cascade hollow-core fibers," *Opt. Lett.* **43**(24), 6009–6012 (2018).